SIMULATING PHOTOSPHERIC DOPPLER VELOCITY FIELDS

DAVID H. HATHAWAY

Space Science Laboratory, NASA Marshall Space Flight Center, Huntsville, AL 35812, U.S.A.

(Received 20 May, 1988)

Abstract. A method is described for constructing artificial data that realistically simulate photospheric velocity fields. The velocity fields include rotation, differential rotation, meridional circulation, giant cell convection, supergranulation, convective limb shift, *p*-mode oscillations, and observer motion. Data constructed by this method can be used for testing algorithms designed to extract and analyze these velocity fields in real Doppler velocity data.

1. Introduction

Artificial data play a crucial role in testing analysis techniques in many scientific disciplines. These data have known characteristics which should produce predictable results from the analysis technique. On the one hand, the artificial data can be extremely simple, so that only one aspect of the analysis is tested. On the other hand, however, some data must be realistic enough to closely match the characteristics of the natural phenomena under investigation.

Artificial data have been used before to simulate Doppler velocity measurements of photospheric flows. For example, Christensen-Dalsgaard (1984) and Balandin, Grigoryev, and Demidov (1987) used a representation of the global oscillation velocities to construct spatial filters for isolating different modes of oscillation. Hathaway (1987) constructed simple velocity fields representing the steady photospheric flows to test a technique for isolating different modes of convection and the large-scale steady flows. However, this earlier work did not allow for a tilt of the Sun's rotation axis toward the observer, did not include components due to the *p*-mode oscillations or the motion of the observer, used the velocity at pixel center rather than an average over the pixel, and did not include a dense and broad spectrum to realistically represent the convective motions such as supergranulation.

With the anticipation of moderate and high resolution Doppler images from the Global Oscillation Network Group (GONG) and the Solar Oscillation Imager (SOI) on the Solar and Heliospheric Observatory (SOHO), artificial data with similar resolution will need to be constructed for testing analysis routines and procedures. A method for producing such data is described in this paper. Section 2 gives an overview of the method. Section 3 provides the practical details for constructing the images and Section 4 presents a candidate spectrum and the resulting images for a realistic simulation of the photospheric motions.

Single Doppler images, like those produced here, can be used to test various algorithms devised for identifying the modes of oscillation or different components of the steady flow. Methods for removing the results of atmospheric seeing and scattering

Solar Physics **117** (1988) 329–341.

or various instrumental effects can be tested by introducing these effects in the images and then comparing corrected images with the originals. A time series of these images could simulate the actual data strings from the GONG or SOI instruments and would be useful for testing techniques for filling data gaps, for merging simultaneous data from different sites, and for testing temporal filters for separating the *p*-mode signal from the steady flow signal. Images produced by the method described below are needed as the first step in many such studies. They represent the pixel averaged velocity as seen by an ideal instrument above the Earth's atmosphere.

2. A Method of Producing Artificial Doppler Images

The vector velocity field on the surface of a sphere can be represented by a spectrum of poloidal and toroidal modes (Chandrasekhar, 1961) with

$$V_r(\theta, \phi) = \sum_{l=0}^{l_{\max}} \sum_{m=0}^{l} R_l^m Y_l^m(\theta, \phi)\,, \tag{1a}$$

$$V_\theta(\theta, \phi) = \sum_{l=1}^{l_{\max}} \sum_{m=0}^{l} \left[S_l^m \frac{\partial Y_l^m(\theta, \phi)}{\partial \theta} + T_l^m \frac{1}{\sin\theta} \frac{\partial Y_l^m(\theta, \phi)}{\partial \phi} \right], \tag{1b}$$

$$V_\phi(\theta, \phi) = \sum_{l=1}^{l_{\max}} \sum_{m=0}^{l} \left[S_l^m \frac{1}{\sin\theta} \frac{\partial Y_l^m(\theta, \phi)}{\partial \phi} - T_l^m \frac{\partial Y_l^m(\theta, \phi)}{\partial \theta} \right], \tag{1c}$$

where $Y_l^m(\theta, \phi)$ is a spherical-harmonic function of degree l and azimuthal order m, θ is the colatitude measured southward from the north pole, and ϕ is the azimuth measured prograde from the central meridian. The complex quantities R_l^m, S_l^m, and T_l^m are the spectral coefficients for the radial, poloidal, and toroidal components, respectively. These coefficients are coupled by the equations of motion for the fluid. Much of the physics to be learned in analyzing the data is concerned with the nature of this coupling and the magnitudes of the various coefficients. Some of the advantages of using this spherical harmonic representation are presented in Appendix A.

To simulate the observed line-of-sight velocity, the spectral coefficients in (1) are specified and the three vector velocity components are calculated and then projected onto the line-of-sight. The result must then be integrated over a picture element (pixel) to simulate the acquisition of Doppler data. The line-of-sight velocity at a point (θ, ϕ) is given with sufficient accuracy by

$$\begin{aligned} V_{\text{los}}(\theta, \phi) = {} & V_r(\theta, \phi) [\sin B_0 \cos\theta + \cos B_0 \sin\theta \cos\phi] + \\ & + V_\theta(\theta, \phi) [\sin B_0 \sin\theta - \cos B_0 \cos\theta \cos\phi] + \\ & + V_\phi(\theta, \phi) [\cos B_0 \sin\phi]\,, \end{aligned} \tag{2}$$

where B_0 is the latitude at disk center (or equivalently the tilt of the Sun's north pole toward the observer) and velocities away from the observer are taken to be positive.

Two other line-of-sight velocity components must be added to this velocity field in order to produce realistic simulations of Doppler images. The convective limb shift, due to the correlation between intensity and velocity in the solar granulation pattern, is not well represented by the spherical harmonic expansion of (1) but is easily expressed as a function of distance from disk center (Andersen, 1984; Cavallini, Ceppatelli, and Righini 1986). The motion of the observer relative to the solar photosphere is also better represented by functions of position on the visible disk rather than functions of heliographic coordinates. The practical details of how these different velocity fields are evaluated and integrated over a pixel to produce a Doppler image are described in the following section.

3. Practical Details for Constructing a Doppler Image

The line-of-sight velocity is calculated by first specifying the spectral coefficients, R_l^m, S_l^m, and T_l^m, and then evaluating the three components of the vector velocity field. This evaluation is done most efficiently by putting the velocity components on a regular grid in colatitude and azimuth and then interpolating to find their values at a particular point on the Doppler velocity image. (Although this grid gives a surplus of points in the polar regions, it is necessary to assure an even sampling of the spherical harmonics and thereby avoid aliasing problems.) The integration of the line-of-sight velocity over a pixel is implemented by dividing the pixel into a number of subpixels, evaluating the line-of-sight velocity at the center of each subpixel, and then averaging.

The functions of the spherical harmonics in (1) can be determined analytically using the recursive relations for the Legendre polynomials (Abramowitz and Stegun, 1964). They give

$$Y_l^m(\theta, \phi) = \bar{P}_l^m(\cos\theta)\, e^{im\phi}\,, \tag{3}$$

$$\frac{\partial}{\partial\theta} Y_l^m(\theta, \phi) = \frac{1}{\sin\theta}\left[lC_{l+1}^m \bar{P}_{l+1}^m(\cos\theta) + (l+1)\, C_l^m \bar{P}_{l-1}^m(\cos\theta)\right] e^{im\phi}\,, \tag{4}$$

and

$$\frac{1}{\sin\theta}\frac{\partial}{\partial\phi} Y_l^m(\theta, \phi) = \frac{1}{\sin\theta} im \bar{P}_l^m(\cos\theta)\, e^{im\phi}\,, \tag{5}$$

where

$$C_l^m \equiv \left[\frac{(l+m)\,(l-m)}{(2l+1)\,(2l-1)}\right]^{1/2}, \tag{6}$$

and $\bar{P}_l^m(\cos\theta)$ is an associated Legendre polynomial normalized so that

$$\int_{-1}^{+1} [\bar{P}_l^m(\cos\theta)]^2\, d(\cos\theta) = 1\,. \tag{7}$$

These expressions for the derivatives are particularly useful in that they only involve Legendre polynomials of the same azimuthal order m. Appendix B describes an efficient means of evaluating the Legendre polynomials for use in these expressions.

The individual components of the vector velocity field are evaluated from the spectral coefficients by first specifying a colatitude point, θ_j, where

$$\theta_j = \pi - (j - \tfrac{1}{2})\frac{\pi}{N_\theta}, \quad j = 1, N_\theta, \tag{8}$$

and then finding the Fourier components at that point by taking the Fourier transform of (1) in the azimuthal direction. This can be done by inspection using (3)–(5) and gives

$$V_r(\theta_j, m) = \sum_{l=m}^{l_{\max}} R_l^m \bar{P}_l^m(\cos\theta_j), \tag{9}$$

$$V_\theta(\theta_j, m) = \frac{1}{\sin\theta_j} \sum_{l=m}^{l_{\max}} S_l^m \left[l C_{l+1}^m \bar{P}_{l+1}^m(\cos\theta_j) - \right.$$

$$\left. - (l+1) C_l^m \bar{P}_{l-1}^m(\cos\theta_j) \right] +$$

$$+ T_l^m \left[im \bar{P}_l^m(\cos\theta_j) \right], \tag{10}$$

and

$$V_\phi(\theta_j, m) = \frac{1}{\sin\theta_j} \sum_{l=m}^{l_{\max}} S_l^m \left[im \bar{P}_l^m(\cos\theta_j) \right] -$$

$$- T_l^m \left[l C_{l+1}^m \bar{P}_{l+1}^m(\cos\theta_j) - (l+1) C_l^m \bar{P}_{l-1}^m(\cos\theta_j) \right]. \tag{11}$$

This part of the calculation can be made more efficient by evaluating (9)–(11) only at points in the northern hemisphere and using the parity properties of the Legendre polynomials for evaluating them at points in the south. These Fourier components are then inverse Fourier transformed to give the velocity at the points

$$\phi_i = (i - 1)\frac{2\pi}{N_\phi}, \quad i = 1, N_\phi. \tag{12}$$

The two other velocity fields, which are represented as functions of position on the Doppler velocity image, must be added before the results can be said to realistically represent a velocity field across the solar disk. The first of these is solar in origin – the convective limb shift. The second results from the motion of the observer relative to the Sun.

The convective limb shift results largely from the correlation between intensity and velocity in the unresolved granulation pattern. It is well represented by functions of distance from disk center (Andersen, 1984; Cavallini, Ceppatelli, and Righini, 1986) but also depends upon the spectral line used in the observation and may depend upon

latitude (Beckers and Taylor, 1980; Brandt and Schröter, 1982) and time (R. K. Ulrich, private communication, 1987). Fluctuations in the granulation pattern will also produce an element of noise in the limb shift signal that varies randomly from pixel to pixel with an amplitude that depends upon the pixel size.

The motion of the observer can be separated into longitudinal motion toward or away from disk center and transverse motion perpendicular to this line. The longitudinal motion is well represented by

$$V_{\text{los}} = c_0(1 - \tfrac{1}{2}\rho^2)\,, \tag{13}$$

where c_0 is the velocity of the observer toward disk center (a function of time) and ρ is the angular distance on the sky from disk center measured in radians. The transverse motion is represented by an apparent rotation of the Sun about an axis perpendicular to the direction of motion and results in a velocity gradient across the disk with

$$V_{\text{los}} = c_x\,\rho \sin\Theta + c_y\,\rho\cos\Theta\,, \tag{14}$$

where c_x and c_y are the components of the observers motion parallel to the solar equator and rotation axis, respectively, and Θ is a position angle measured clockwise from the heliographic north.

The line-of-sight velocity is constructed from these individual velocity components. Each pixel is divided into an array of subpixels. The line-of-sight velocity is then calculated from (2) by finding the coordinates (θ, ϕ) at the center of the subpixel and interpolating from adjacent points using a second order accurate scheme, e.g.,

$$\begin{aligned} V(\theta,\phi) = {} & V(\theta_j,\phi_i) + \\ & + \tfrac{1}{2}\left[V(\theta_{j+1},\phi_i) - V(\theta_{j-1},\phi_i)\right]\Delta\theta + \\ & + \tfrac{1}{2}\left[V(\theta_{j+1},\phi_i) - 2V(\theta_j,\phi_i) + V(\theta_{j-1},\phi_i)\right]\Delta\theta^2 + \\ & + \tfrac{1}{2}\left[V(\theta_j,\phi_{i+1}) - V(\theta_j,\phi_{i-1})\right]\Delta\phi + \\ & + \tfrac{1}{2}\left[V(\theta_j,\phi_{i+1}) - 2V(\theta_j,\phi_i) + V(\theta_j,\phi_{i-1})\right]\Delta\phi^2\,, \end{aligned} \tag{15}$$

where

$$\Delta\theta = (\theta - \theta_j)\frac{N_\theta}{\pi}, \tag{16}$$

and

$$\Delta\phi = (\phi - \phi_i)\frac{N_\phi}{2\pi}. \tag{17}$$

Values for points beyond the boundaries are easily obtained since the boundaries of the velocity arrays map back onto themselves. The limb shift and observer motion are then added and the line-of-sight velocity for an image pixel is given by a simple average over all subpixels that map onto the disk.

4. A Realistic Example

Velocity images have been constructed with this method to test data analysis and reduction algorithms that will be used on data from the GONG and SOI instruments. Simple, single component images have been made for testing mode identification routines. In addition, a substantial amount of effort has been devoted to making quite realistic images by specifying a broad spectrum for the coefficients R_l^m, S_l^m, and T_l^m (specified in units of m s^{-1}). This spectrum was used to construct velocity images on a 256 × 256 pixel array for which it was assumed that the image scale was 2000″ across 256 pixels. The arrays for the vector velocity components each had 256 points in colatitude and 512 points in azimuth. The time of 'observation' was arbitrarily chosen to be 17 : 00 UT on 1 August, 1985. This set the latitude at disk center, giving $B_0 = 5.69°$, and set the radius of the image, giving a semi-diameter of 947.04″. Each pixel in the image was divided into a 4 × 4 array of subpixels for averaging. In making these velocity images it was assumed that the velocity field due to the *p*-mode oscillations is purely radial while that due to the steady flows is purely in the horizontal. Although the chosen spectrum is not unique in its ability to mimic the observed velocity fields, it has an advantage in being fairly simple.

The *p*-mode spectrum was given by a uniform amplitude for all modes up to a cutoff at $l = 354$. Although the higher degree modes are probably not well resolved by the 256 × 256 image, a comparison with an image produced on a 512 × 512 array shows that the final images agree quite well. The amplitude of the line-of-sight velocity matches the observations when a 1 m s^{-1} amplitude was used for the modes with

$$R_l^m = 1 \cdot e^{i\Phi}, \tag{18}$$

where Φ is a random phase for each mode, l extends from 0 to 354, and m extends from 0 to l. When summed over m this gives a spectrum that increases linearly with l and produces a Doppler velocity image that has no preferred position or orientation. Figure 1 shows a representative image for a given set of random phases. The pattern agrees quite well with the observations of Leighton, Noyes, and Simon (1962). It has a fairly random and small cell size with an amplitude of about 300 m s^{-1} and the signal vanishes near the limb because of projection effects.

The steady flow spectrum was characterized by four different types of flow: rotation, meridional circulation, giant convection cells, and supergranulation convection cells. The rotation and differential rotation are axisymmetric ($m = 0$) toroidal flows. A three-component spectrum was used with

$$T_1^0 = 1569.585, \tag{19}$$

$$T_3^0 = -33.070, \tag{20}$$

and

$$T_5^0 = -3.444. \tag{21}$$

This gives a rotation profile nearly identical to that of Howard and Harvey (1970). More

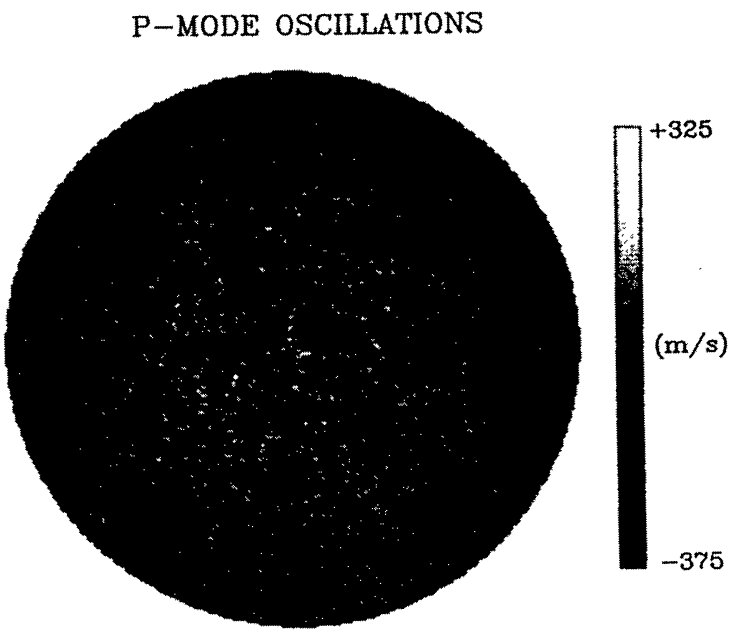

Fig. 1. A Doppler velocity image for the *p*-mode oscillations. Dark areas are approaching the observer; light areas are receding. The pattern shows fairly random variations with an amplitude of about 300 m s^{-1} which diminishes near the limb due to projection effects.

recent rotation profiles might be used and the torsional oscillation signal might also be included. The primary concern is that the rotation profile for the simulation is accurately known and should be accurately recovered by analysis techniques designed to determine the profile.

The meridional circulation is an axisymmetric ($m = 0$) poloidal flow. Considerable controversy exists concerning the nature of the meridional circulation on the Sun so a somewhat arbitrary spectrum was used with

$$S_2^0 = 8.433 \tag{22}$$

and

$$S_4^0 = 2.236\,. \tag{23}$$

This gives a meridional flow that is directed toward the poles from the equator but with latitudinal variations in the velocity amplitude that would imply (from the equation of mass continuity) a downflow at mid-latitudes.

Controversy also exists concerning the giant cells so another somewhat arbitrary spectrum was used. This spectrum extends from $l = 1$ to $l = 24$, has a peak at $l = 12$, and includes azimuthal orders $m = 1$ to $m = l$. The poloidal and toroidal components for each l and m are of equal amplitude and in phase with each other but random phases are taken for successive modes. This spectrum is given by

$$S_l^m = \frac{1}{l}\left[1 - \frac{(l-12)^2}{12^2}\right] e^{i\Phi}, \quad l = 1, 24, \tag{24}$$

and

$$T_l^m = S_l^m. \tag{25}$$

The large toroidal component was included because solar rotation should be a strong influence on these large scale, low amplitude flows. Numerical modelling (Glatzmaier, 1984; Gilman and Miller, 1986) suggests a highly anisotropic giant cell pattern with cells elongated north to south across the equator dominated by modes with $l \sim 12$, the spectrum given by (24) and (25) has a similar peak but is independent of m and produces a more cellular pattern.

The spectrum for the supergranules is fairly well constrained by observations. Taking 3×10^4 km as a characteristic size for supergranules (Leighton, Noyes, and Simon 1962) indicates $l \sim 150$. Several spectra with peaks about $l = 150$ were used and it was found that a large spectral width was required to produce a pattern similar to that observed for supergranules. The adopted spectrum extends from $l = 70$ to $l = 230$ with $m = 1$ to $m = l$. Since the convective motions in supergranules are expected to be only weakly influenced by solar rotation (Hathaway, 1982), the toroidal components were taken to be only a tenth as large as the poloidal components. This spectrum is given by

$$S_l^m = \frac{5}{l}\left[1 - \frac{(l-150)^2}{80^2}\right] e^{i\Phi}, \quad l = 70, 230, \tag{26}$$

and

$$T_l^m = \tfrac{1}{10} S_l^m. \tag{27}$$

The full spectrum for the steady flow component is shown in Figure 2.

Figure 3 shows the line-of-sight velocity pattern for the supergranules and for the giant cells. The supergranule pattern compares quite favorably with observations (e.g., Durney *et al.*, 1985, Figure 1). The pattern is cellular with approaching velocities alternating with receding velocities and the zero velocity lines are largely parallel to the limb. The pattern vanishes near disk center because the velocities were taken to be purely horizontal, and vanishes near the limb due to averaging over foreshortened cells. The maximum velocities are on the order of 500 m s^{-1} which also agrees well with observations (Leighton, Noyes, and Simon 1962). The giant cell pattern has a much lower amplitude but with a larger cell size. The zero velocity lines are not parallel to the limb for the giant cells and produce an apparent spiral pattern about disk center because of the large toroidal component of the flow.

For the total velocity field a convective limb shift was included in the data with

$$V_{\text{los}} = -547.79 + 175.79(1-\mu) + 101.60(1-\mu)^2 + \\ + 270.40(1-\mu)^3 \text{ m s}^{-1}, \tag{28}$$

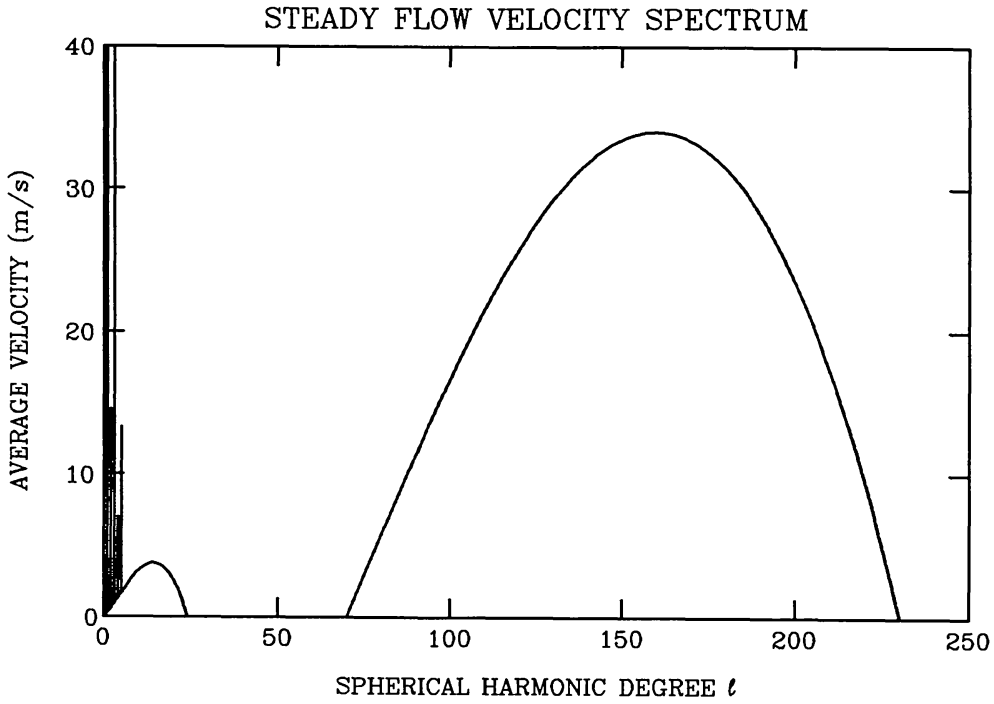

Fig. 2. Velocity spectrum for the steady flow components in the synthetic data. The root-mean-squared velocity in the horizontal motions averaged over the surface of the Sun and summed over all orders m is plotted as a function of spherical harmonic degree l. Rigid rotation, with $l = 1$ and average velocity 1569.6, goes off the vertical scale of this plot. Differential rotation is represented by the spikes at $l = 3$ and $l = 5$. The $l = 3$ component has an average velocity of 81.0 and also goes off scale. The meridional circulation is represented by spikes at $l = 2$ and $l = 4$. Supergranules are represented by the broad peak about $l = 150$ and giant convection cells are represented by the peak about $l = 12$.

where μ is the cosine of the heliocentric angle from disk center (Cavallini, Ceppatelli, and Righini, 1986). The motion of a hypothetical observer at Sacramento Peak, New Mexico was also included with

$$V_{\text{los}} = -421.14(1 - 0.5\rho^2) - 28931.2\rho \sin\Theta - \\ - 2190.3\rho\cos\Theta \text{ m s}^{-1}, \tag{29}$$

where ρ is measured in radians (T. Brown, private communication, 1987). The resulting line-of-sight velocity image is shown in Figure 4.

5. Conclusions

Realistic data have been constructed with the method described in the preceding sections. The line-of-sight velocity field presented in Figure 4 has many characteristics in common with actual Doppler images of the Sun. Artificial data such as this can be used to test algorithms and analysis routines used for reducing Doppler velocity data from instruments like those proposed for GONG and SOHO. Simpler images are, of

Third, the kinetic energy associated with the motions is simply expressed by

$$KE(r) \equiv \frac{1}{2}\rho(r)\frac{1}{4\pi}\int_0^{\pi}\int_0^{2\pi} [V_r^2(\theta,\phi) + V_\theta^2(\theta,\phi) + V_\phi^2(\theta,\phi)]\,\mathrm{d}\phi\sin\theta\,\mathrm{d}\theta =$$

$$= \tfrac{1}{4}\rho(r)\{[R_l^m]^2 + l(l+1)[S_l^m]^2 + l(l+1)[T_l^m]^2\}\,. \tag{A.3}$$

So the kinetic energy and average velocity of each individual mode can be easily determined. Fourth, the angular momentum of the surface about the pole is simply expressed by

$$L(r) \equiv r^3\,\rho(r)\int_0^{\pi}\int_0^{2\pi} [\sin\theta\, V_\phi(\theta,\phi)]\,\mathrm{d}\phi\sin\theta\,\mathrm{d}\theta =$$

$$= [4\pi r3\,\rho(r)]\sqrt{\tfrac{2}{3}}\,T_1^0\,. \tag{A.4}$$

So a single spectral component specifies the total angular momentum of the surface.

It should be noted that the spherical harmonics can represent the axisymmetric flows such as differential rotation and meridional circulation with the same ease and efficiency as other often used methods (such as power series in $\sin(B)$). The spherical harmonic representation is preferred for reasons of interpretation.

Appendix B

In producing the velocity images a series of associated Legendre polynomials of azimuthal order m and degrees $l = m$ to $l = l_{\max}$ at a colatitude point θ are required. This same situation arises in taking a spherical harmonic transform. The data undergo a Fourier transform in azimuth and then require a series of Legendre transforms for each azimuthal order m. This can be done most efficiently using the recurrence relation

$$\bar{P}_l^m(\cos\theta) = A_l^m\cos\theta\bar{P}_{l-1}^m(\cos\theta) - B_l^m\bar{P}_{l-1}^m(\cos\theta)\,, \tag{B.1}$$

where

$$A_l^m = \left[\frac{(2l+1)(2l-1)}{(l+m)(l-m)}\right]^{1/2}, \tag{B.2}$$

and

$$B_l^m = \left[\frac{(2l+1)(l+m+1)(l-m-1)}{(2l-3)(l+m)(l-m)}\right]^{1/2}. \tag{B.3}$$

This generates each of the required polynomials in turn, without calculating any other unnecessary terms. The coefficients A_l^m and B_l^m (as well as C_l^m as defined by (6)) can be calculated once and stored for repeated use at each colatitude point. The starting

course, much easier to produce and provide a powerful means of testing data reduction programs.

The images produced with this method represent the line-of-sight velocity at an array of pixels on a solar image from an ideal instrument above the atmosphere. The method as described here does not include the effects of atmospheric scattering and seeing or any of the instrumental effects involved in measuring this velocity field. Efforts to include these effects have been undertaken by other members of the GONG Artificial Data Project Team for the proposed GONG instrument. Using images like that shown in Figure 4 as originals, this project has produced realistic simulations of observations with the GONG instruments. A time series of such images is planned for the near future for testing data merging, gap filling, and temporal filtering algorithms.

The FORTRAN program written to produce the data shown in Figure 4 requires about 1 hr of cpu time on a VAX 8300 or about 30 s on a CRAY X-MP. Thus, single images can be readily produced and modest time strings are also possible. This program is available through the GONG for use by the community.

Acknowledgements

Support for this research was provided by the NASA Office of Solar Physics. The author would like to thank Steve Suess and Tauna Moorehead for their comments and suggestions on the manuscript and Ed Reichmann and James Smith for their help with the figures. The author is also very grateful for many useful discussions with members of the GONG Artificial Data Project Team including Bo Andersen at ESA, Tim Brown at HAO, and John Leibacher and Frank Hill at NSO.

Appendix A

There are several advantages to representing the velocity field in terms of normalized spherical harmonics as in (1) First, the normalized spherical harmonics comprise a complete orthonormal set of functions on a sphere with

$$\frac{1}{2\pi}\int_0^{\pi}\int_0^{2\pi} Y_{ml}(\theta,\phi)\,Y_k^n(\theta,\phi)\,\mathrm{d}\phi\,\sin\theta\,\mathrm{d}\theta = \delta_l^k\delta_m^n\,, \tag{A.1}$$

and as such are the preferred basis for representing a field quantity. Second, if the velocity is solenoidal (e.g., Chandrasekhar, 1961) the radial and poloidal coefficients are coupled with

$$\frac{1}{r^2}\frac{\partial}{\partial r}[r^2 R_l^m] = -\frac{l(l+1)}{r}S_l^m\,. \tag{A.2}$$

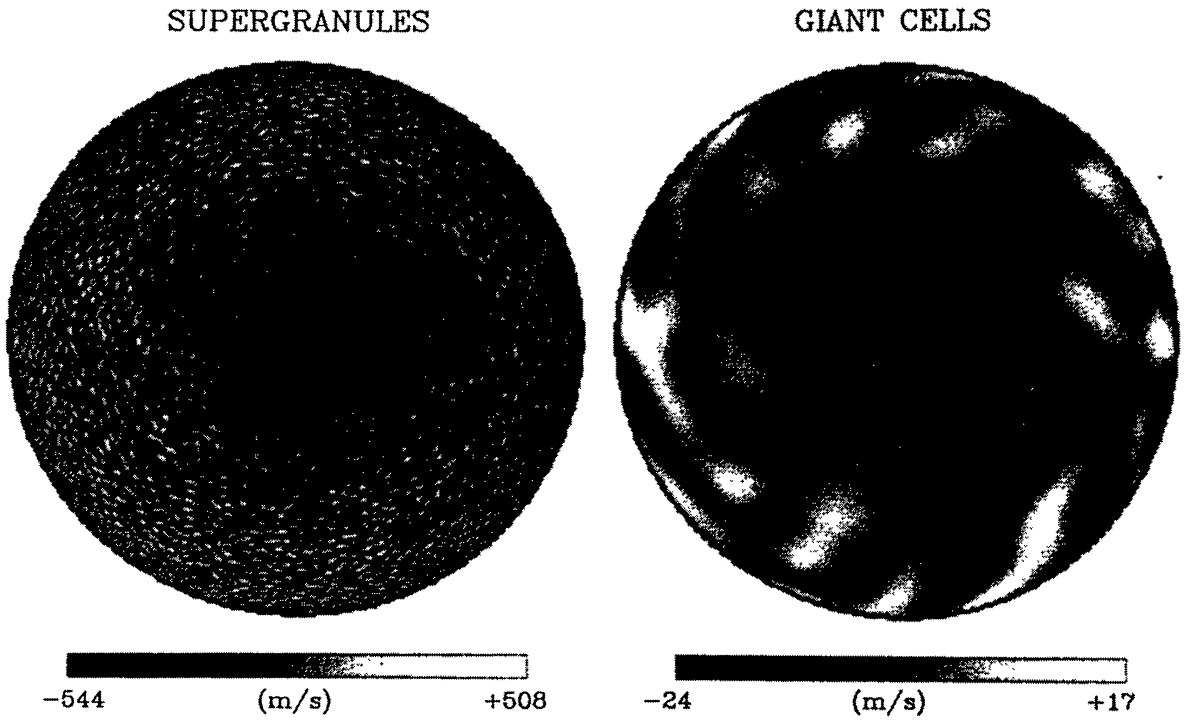

Fig. 3. The resultant line-of-sight velocity field for the supergranules and the giant cells. Dark areas are approaching the observer; light areas are receding. The supergranule pattern is cellular with peak amplitudes of about 500 m s^{-1} near the limb. The giant cell pattern has much larger cells but with peak amplitudes of only about 20 m s^{-1}.

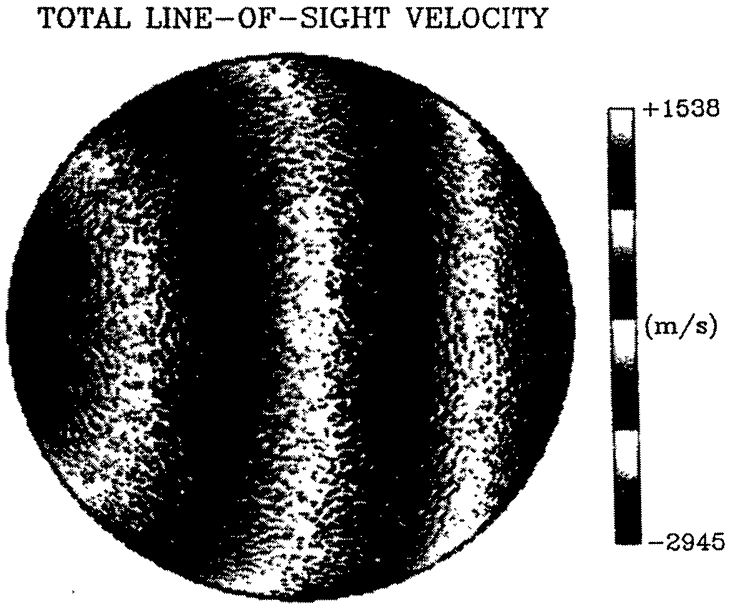

Fig. 4. The total line-of-sight velocity field constructed from the candidate spectrum. Rotation, supergranulation, limb shift, and *p*-modes are noticeable. The giant cells and meridional circulation, having smaller amplitudes, are masked by these stronger components. The velocity scale passes from dark to light four times to help bring out the cellular patterns.

values for the relation are

$$\bar{P}_m^m(\cos\theta) = \left[\frac{1}{2}\frac{3\cdot 5\cdot 7\ldots(2m+1)}{2\cdot 4\cdot 6\ldots(2m)}\right]^{1/2} \sin^m\theta\,, \tag{B.4}$$

and

$$\bar{P}_{m-1}^m(\cos\theta) = 0\,. \tag{B.5}$$

While this scheme is stable and efficient, it does require the use of extended range arithmetic as described by Smith, Olver, and Lozier (1981) to accommodate the large, negative exponents that arise when m becomes large.

The recurrence relation given by (B.1) is preferred to those suggested by Libbrecht (1985). In producing and analysing data like this one needs to generate a series of Legendre polynomials with a given azimuthal order m for degrees $l = m$ to some maximum value. The relation (B.1) does this with three multiplications and one addition for each increment in l. The recurrence relations suggested by Libbrecht require a long series of such operations that generate many intermediate results that are either discarded or stored in large arrays.

References

Abramowitz, M. and Stegun, I. A.: 1964, *Handbook of Mathematical Functions*, Natl. Bureau of Standards.
Andersen, B. N.: 1984, *Solar Phys.* **94**, 49.
Balandin, A. L., Grigoryev, V. M., and Demidov, M. L.: 1987, *Solar Phys.* **112**, 197.
Beckers, J. M. and Taylor, W. R.: 1980, *Solar Phys.* **68**, 41.
Brandt, P. N. and Schröter, E. H.: 1982, *Solar Phys.* **79**, 3.
Cavallini, F., Ceppatelli, G., and Righini, A.: 1986, *Astron. Astrophys.* **163**, 219.
Chandrasekhar, S.: 1961, *Hydrodynamic and Hydromagnetic Stability*, Oxford.
Christensen-Dalsgaard, J.: 1984, in R. K. Ulrich (ed.), *Solar Seismology from Space*, JPL, Pasadena, p. 209.
Durney, B. R., Cram, L. E., Guenther, D. B., Keil, S. L., and Lytle, D. M.: 1985, *Astrophys. J.* **292**, 752.
Gilman, P. A. and Miller, J.: 1986, *Astrophys. J. Suppl.* **61**, 585.
Glatzmaier, G. A.: 1984, *J. Comput. Phys.* **55**, 461.
Hathaway, D. H.: 1982, *Solar Phys.* **77**, 341.
Hathaway, D. H.: 1987, *Solar Phys.* **108**, 1.
Howard, R. and Harvey, J.: 1970, *Solar Phys.* **12**, 23.
Leighton, R. B., Noyes, R. W., and Simon, G. W.: 1962, *Astrophys. J.* **135**, 474.
Libbrecht, K. G.: 1985, *Solar Phys.* **99**, 371.
Smith, J. M., Olver, F. W. J., and Lozier, D. W.: 1981, *ACM Trans. Math. Software* **7**, 93.
Ulrich, R. K.: 1987, private communication.